

## Article

# ~25 Ma Ruby Mineralization in the Mogok Stone Tract, Myanmar: New Evidence from SIMS U–Pb Dating of Coexisting Titanite

Di Zhang <sup>1,2</sup>, Shun Guo <sup>1,3,\*</sup>, Yi Chen <sup>1,3</sup> , Qiuli Li <sup>1</sup> , Xiaoxiao Ling <sup>1</sup>, Chuanzhou Liu <sup>1</sup>  and Kyaing Sein <sup>4</sup>

- <sup>1</sup> State Key Laboratory of Lithospheric Evolution, Institute of Geology and Geophysics, Chinese Academy of Sciences, Beijing 100029, China; zhangdi@mail.iggcas.ac.cn (D.Z.); chenyi@mail.iggcas.ac.cn (Y.C.); liqiuli@mail.iggcas.ac.cn (Q.L.); lingxx@mail.iggcas.ac.cn (X.L.); chzliu@mail.iggcas.ac.cn (C.L.)
- <sup>2</sup> College of Earth and Planetary Sciences, University of Chinese Academy of Sciences, Beijing 100049, China
- <sup>3</sup> Chinese Academy of Sciences Center for Excellence in Tibetan Plateau Earth Sciences, Beijing 100101, China
- <sup>4</sup> Myanmar Geosciences Society, Hlaing University Campus, Yangon 11041, Myanmar; kyaingsein@gmail.com
- \* Correspondence: guoshun@mail.iggcas.ac.cn; Tel.: +86-010-8299-8534

**Abstract:** Ruby (red corundum) is one of the most prominent colored gemstones in the world. The highest-quality ruby (“pigeon blood” ruby) comes from marbles of the Mogok Stone Tract in central Myanmar. Although Mogok ruby has been exploited since the 6th century AD, the formation time of this gemstone is ambiguous and controversial. In this paper, we describe a mineralogical, geochemical, and geochronological study of ruby and titanite in ruby-bearing marbles obtained from an outcrop in the Mogok Stone Tract, central Myanmar. Petrographic observations have shown that titanite generally occurs in the marble matrix or occurs as inclusions in ruby. These two types of titanite exhibit identical chemical compositions. In situ secondary ion mass spectrometer (SIMS) U–Pb dating of the separated titanite from two representative samples of ruby-bearing marbles yielded lower intercept ages of  $25.15 \pm 0.24$  Ma (MSWD = 0.26) and  $25.06 \pm 0.22$  Ma (MSWD = 0.15), respectively. Because the closure temperature of the U–Pb system in titanite is close to the temperature of ruby growth, the obtained U–Pb ages (~25 Ma) are suggested to represent the timing of the studied ruby formation in Mogok. The acquired ages are in agreement with the timing of post-collisional extension in the Himalaya related to the migration of the eastern Himalayan syntaxis. Combining our dating results with previous geochronological data from the Mogok Stone Tract, we suggest that the formation of the studied ruby is most likely related to the high-temperature metamorphic event in the marbles during the India–Asia collision. Our study not only confirms that texturally constrained titanite could be a precise geochronometer to date the mineralization of different types of ruby, but also provides important geochronological information linking gemstone formation to the India–Asia collision.

**Keywords:** ruby; titanite; Mogok Stone Tract; SIMS; India–Asia collision



**Citation:** Zhang, D.; Guo, S.; Chen, Y.; Li, Q.; Ling, X.; Liu, C.; Sein, K. ~25 Ma Ruby Mineralization in the Mogok Stone Tract, Myanmar: New Evidence from SIMS U–Pb Dating of Coexisting Titanite. *Minerals* **2021**, *11*, 536. <https://doi.org/10.3390/min11050536>

Academic Editor: Frederick Lin Sutherland

Received: 28 April 2021  
Accepted: 10 May 2021  
Published: 19 May 2021

**Publisher’s Note:** MDPI stays neutral with regard to jurisdictional claims in published maps and institutional affiliations.



**Copyright:** © 2021 by the authors. Licensee MDPI, Basel, Switzerland. This article is an open access article distributed under the terms and conditions of the Creative Commons Attribution (CC BY) license (<https://creativecommons.org/licenses/by/4.0/>).

## 1. Introduction

Ruby, a red variety of Cr-bearing corundum ( $Al_2O_3$ ), is the most prominent and valuable colored gemstone because of its extraordinary appearance and rare occurrence [1,2]. Due to its unique “pigeon blood” color, ruby from the Mogok Stone Tract (central Myanmar) represents the highest grade of corundum gemstone worldwide [2]. In 2015, a Mogok ruby of 25.59 carats (~5.1 g) named “The Sunrise Ruby” broke the record for the world’s most expensive colored gemstone with a hammer price of more than 30 million dollars [3]. Mogok ruby crystals are found exclusively in marbles and associated calc-silicate rocks [4,5]. Although Mogok rubies have been exploited for several hundred years, the formation process of this gemstone and its association with the India–Asia collision are highly ambiguous and controversial [2,4–7]. Precise dating of ruby formation plays a crucial role

in understanding its genesis. Several factors make the dating of mineralization in the Mogok Stone Tract highly challenging: (1) foreigners were strictly forbidden from visiting the Mogok mines until 2012 [8], so most reported samples have been obtained from gem markets or museums; thus, direct information on the field relationships and petrographic textures of ruby-bearing rocks is usually not available; (2) the host metacarbonate rocks of ruby are notoriously difficult to date due to a lack of suitable chronometers [9]; (3) “hard” ruby typically occurs as isolated, rigid crystals in a “soft” carbonate matrix, which makes it difficult to maintain original ruby crystals during the process of making thin sections; thus, the coexisting relationship between ruby and other silicate/oxide minerals (especially accessory minerals) is difficult to determine [4,7]. To date, the formation ages of ruby are speculated via  $^{40}\text{Ar}$ – $^{39}\text{Ar}$  dating of phlogopite in ruby-bearing marbles ( $18.7 \pm 0.2$  Ma) [6] and U–Pb dating of inclusions in ruby crystals (31–32 Ma and 22 Ma for zircon; 32.4 Ma and 21 Ma for titanite) [7,8,10–12]. However, the  $^{40}\text{Ar}$ – $^{39}\text{Ar}$  dating result may represent a younger age than the ruby formation time due to the lower closure temperature of phlogopite [6,13], and the zircon inclusions may have the potential to be detrital grains inherited from the protoliths of the marbles. Thus, more geochronological data from the Mogok belt are strongly needed to better understand ruby genesis.

Titanite is a common accessory mineral in Ca-rich metamorphic rocks [14]. This mineral can contain high field-strength elements, such as Zr, Nb, and Ta (substitutions for Ti site), and rare earth elements (REEs, substitutions for Ca site), which provide significant information for understanding igneous, metamorphic, and ore-forming processes [14]. Moreover, the ability to incorporate quantities of U, Th, and Pb into the lattice (substitutions for Ca site) makes titanite an ideal U–Th–Pb geochronometer [14–19]. Metamorphic processes with a wide range of temperatures can be constrained well by titanite U–Pb dating using modern microbeam techniques such as laser ablation inductively coupled plasma mass spectrometry (LA-ICP-MS) or SIMS [20–22]. Furthermore, the U–Pb system in titanite has a relatively high closure temperature (approximately 650–700 °C) [14], close to the formation temperatures of gem-quality corundum in marble (620–670 °C) [23], which suggests that titanite, if present, could be an appropriate mineral to constrain the age of ruby formation. Although titanite has previously been reported in many ruby-bearing marbles [1,2,4,5,8], the paragenetic relationship of titanite and ruby has rarely been examined, thus hindering attempts to employ titanite as a chronometer of ruby formation.

In this study, we investigated two representative samples of ruby-bearing metacarbonate rocks from the outcrop of the Mogok Stone Tract, central Myanmar. The occurrences, textures, and chemical compositions of ruby and titanite in the two samples were carefully examined. In addition, the U–Pb isotopes ages of titanite were acquired by SIMS, and the precise timing of ruby mineralization was determined. Our results provide important data for the study of ruby formation in the Mogok Stone Tract and confirm that titanite is an ideal mineral for the age determination of gemstones and metamorphism in marble.

## 2. Geological Setting and Sample Description

Myanmar, located in the southeast of Asia, is geologically divided into the Indo-Burma Ranges, Central Basin, Mogok Metamorphic Belt (MMB), and Shan Plateau. The N–S striking, 1200 km long, right-lateral strike-slip Sagaing fault runs most of the length of Myanmar and cuts the western margin of the MMB [24–29]. Between the Sagaing fault and Shan Plateau lies the MMB, which extends for approximately 1500 km from the Andaman Sea north to the eastern Himalayan syntaxis (Figure 1a) [7,26,28–31]. The MMB has experienced a complex evolution related to the closure of the Tethyan Ocean and the collision of India with Asia, including sedimentation and drifting >200 Ma ago; subsequent multistage plate subduction and continental collision; and postcollision extension, shearing, and uplift accompanied by the intrusion of large-scale magmatic rocks [5]. Previous age determinations indicate that metamorphism occurred during the Tertiary, with ages ranging from 68 Ma to 21 Ma [8,26,32–34]. Peak granulite-facies metamorphism along the MMB occurred mainly between the Middle Eocene and the early Oligocene [8,26,33,34]. Metamorphic

rocks in the MMB, including schists, gneisses, migmatites, gem-bearing (ruby and spinel) marbles, calc-silicate rocks, and quartzites, formed under amphibolite- to granulite-facies conditions [25,26,32]. Intrusions of syenite, granitoid bodies, and leucosomes, dikes, hydrothermal veins, and pegmatites can be found in the MMB e.g., [8,31,32]. Metasomatic skarns occur in contact zones between the marbles and intrusions as a function of the infiltration of fluids/melts. Metasomatism may form various mineralogical reaction zones in which rare gems are produced [5,8,30,35].

The Mogok Stone Tract is located at the northeastern edge of the MMB and hosts world-class deposits of ruby, sapphire, spinel, and other gemstones. The main lithologies exposed in the vicinity of Mogok are marbles, some gem-bearing (ruby, sapphire, and spinel), garnet-sillimanite paragneisses, and calc-silicate rocks, representing a regional high-temperature metamorphic unit. Conventional geothermobarometer estimated peak P–T conditions are 6–10 kbar and 780–850 °C for Mogok granulites [36–38]. These metamorphic rocks are intruded by alkaline igneous rocks (Oligocene–early Miocene sodic nepheline-syenite and syenite-pegmatite and urtite suites) [8,12,39] and early Oligocene leucogranites [12]. A large leucogranite intrusion, the Kabaing granite, dated at  $16.8 \pm 0.5$  Ma (U–Pb zircon), intrudes the Mogok marbles and syenites [40]. The Kabaing granitoids and metasedimentary rocks are commonly intruded by late-stage pegmatites and aplites [41]. Gem-quality ruby is widely distributed in the primary deposits and secondary deposits in the Mogok area [42].

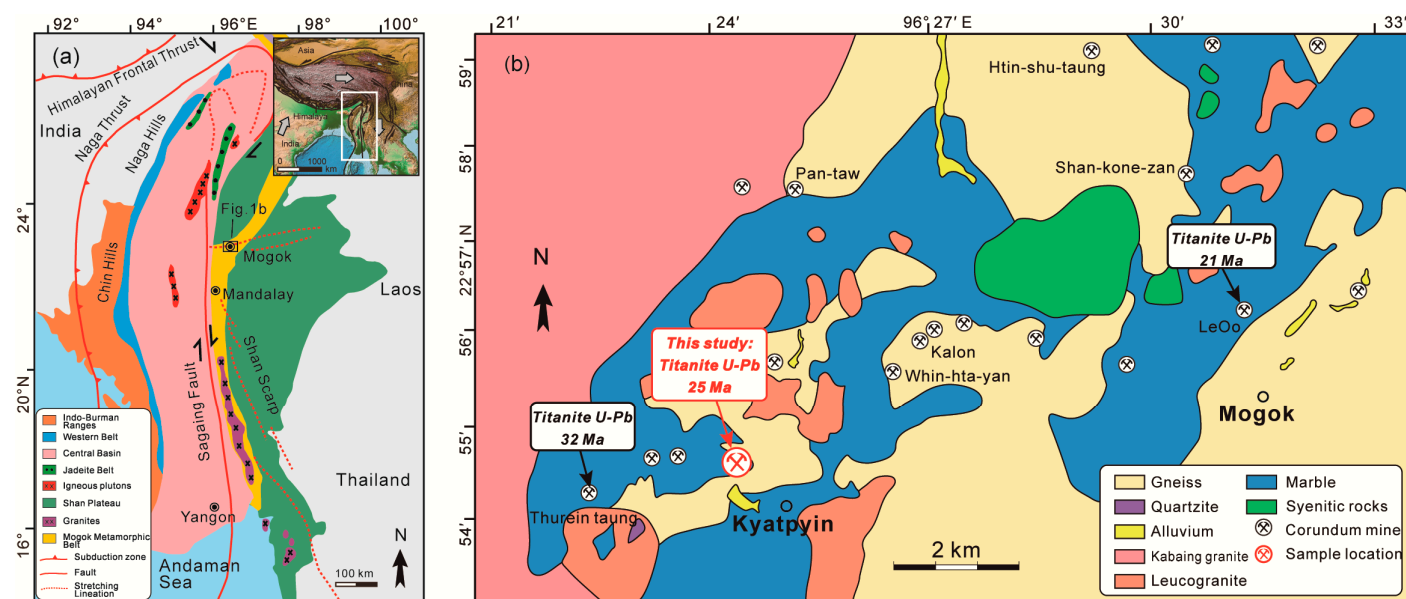


**Figure 1.** (a) Geological sketch map of Myanmar, modified after Guo et al. [30]. (b) A simplified geological map of the Mogok region (modified from Zaw et al. [43]) showing the distribution of various lithologies and the location of the studied samples.

Several recent geochronological studies on ruby formation time in the Mogok Stone Tract have been published. Garnier et al. [6] first reported the  $^{40}\text{Ar}$ – $^{39}\text{Ar}$  dating results of phlogopite in ruby-bearing marbles ( $18.7 \pm 0.2$  Ma). Additionally, a zircon U–Pb date of 16.1 Ma was reported in a painite ( $\text{CaZrAl}_9\text{O}_{15}(\text{BO}_3)$ ) overgrowth on ruby in a skarn contact between leucogranite and marble (Wet Loo mine [39]). Zaw et al. [10,11] provided an age of 31–32 Ma by U–Pb dating of zircon inclusions in Mogok ruby. Sutherland et al. [12] reported U–Pb dating results of titanite and zircon inclusions in ruby from Thurein Taung, determined via LA-ICP-MS. Seven analyses of a single titanite grain provided an intercept age of ~32 Ma, which matches the age of leucocratic granite bodies intruding this area. However, three zircons included in the same ruby megacryst provided a range of older ages from ~50 to ~100 Ma. The adjacent syenite indicated a U–Pb zircon date of 25 Ma [12,39]. Through detailed field work in the Mogok valley, Searle et al. [8] found that ruby was

spatially related to a series of charnockite-syenite sill-like intrusions around the Mogok valley. The U–Pb titanite ages from the ruby marbles and skarns at the Le Oo mine were ~21 Ma, which were similar to the titanite ages from an adjacent syenite (22 Ma). Phyo et al. [7] performed detailed research on zircon inclusions in Mogok ruby and found that zircon grains displayed growth zoning (core/rim) structures. To acquire the precise ages of small zircon grains with the simultaneous acquisition of the full mass spectrum, they carried out U–Pb dating using both sector-field mass spectrometry (LA-ICP-SF-MS) and laser ablation inductively coupled plasma time-of-flight mass spectrometry (LA-ICP-TOF-MS). The zircon core displayed a wide range of ages (~94 to ~26 Ma). However, individual spots from zircon rims revealed ages between ~30 Ma and ~22 Ma. The youngest ages were concordant at  $22.26 \pm 0.36$  Ma for rims of zircon inclusions and were interpreted as the ruby formation time.

The investigated samples (ruby-bearing marbles 13MK79 and 13MK80) in this study were collected from an abandoned mine near Kyatpyin in the Mogok Stone Tract (GPS: 96°24'28" E, 22°54'34" N, Figure 1b). The ruby-bearing marbles were mainly composed of calcite (>96 vol.%), diopside (<1 vol.%), and dolomite (~0.5 vol.%), with minor amounts of silicate minerals (plagioclase, phlogopite, K-feldspar, scapolite, titanite, <1.5 vol.%), ruby (<0.5 vol.%), and pyrite (<0.5 vol.%) (Figure S1). Ruby occurred as red to deep pink, subhedral to euhedral crystals in the marbles, with grain sizes ranging from 0.02 to 1 cm (Figure 2b–d). The ruby typically contained inclusions of calcite, titanite, apatite, and zircon (Figure 2e–g). Anhedral titanite grains generally occurred in the marble matrix or occurred as inclusions in ruby and other silicate minerals (Figure 2e,g,h and Figure S1). Matrix titanite grains were relatively large (typically more than several hundred microns) (Figure 2h). The sizes of titanite inclusions in the ruby varied greatly, ranging from 20 to >300  $\mu\text{m}$  (Figure 2e,g). No zonation was found in the titanite. Calcite may occur as a matrix mineral (Figure 2d), and its size generally ranged from 0.2 to 3.0 mm. In addition, calcite occurred in some cases as inclusions in ruby 10–100  $\mu\text{m}$  in size (Figure 2e,f). Anhedral clinopyroxene, dolomite, and flaky phlogopite also occurred as matrix minerals (Figure S1).

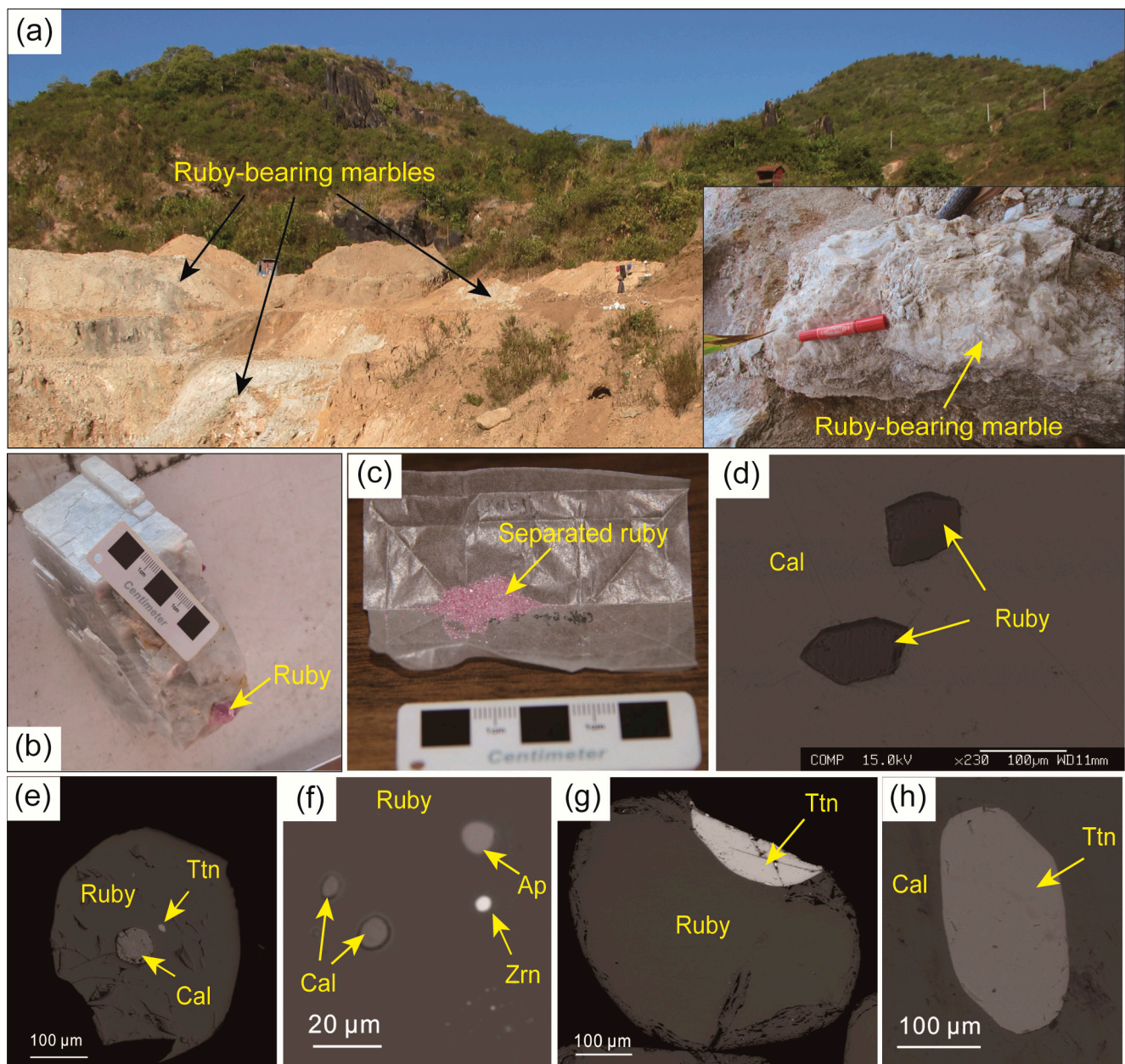


**Figure 2.** Field views (a) specimen photographs (b,c) and backscattered electron images (d–h) showing the occurrence of ruby-bearing marbles and the textural characteristics of ruby crystals. (a) Field views of ruby-bearing marbles. Inserted image showing the investigated coarse-grained marbles. (b) Deep pink ruby crystal in the marble. (c) Ruby grains separated from the ruby-bearing marble. (d) Subhedral to euhedral ruby crystals in the coarse-grained marble. (e) Calcite and tiny titanite inclusions in ruby. (f) Small calcite, apatite, and zircon inclusions in ruby. (g) Titanite inclusion in ruby. (h) Anhedral titanite without sector zones in marble. Mineral abbreviations [44]: Cal, calcite; Ttn, titanite; Ap, apatite; Zrn, zircon.

### 3. Analytical Methods

#### 3.1. Whole-Rock Major and Trace Elements

Two marble samples (13MK79 and 13MK80) were first disaggregated into small blocks. After being cleaned in an ultrasonic cleaner and placed in the oven at 60 °C for more than 24 h, these blocks were ground in an agate mill to approximately 200 mesh for whole-rock analysis.

Whole-rock analyses were conducted at ALS Chemex Co., Ltd. in Guangzhou, China. Major element oxides were measured on fused glass disks using a Phillips PW 1500 X-ray

fluorescence spectrometer (XRF, PANalytical, Almelo, The Netherlands) with better than 5% analytical precision. Loss on ignition (LOI) was analyzed after heating to 1000 °C. The FeO content was acquired via titration with potassium dichromate [45].

Whole-rock trace element compositions were obtained using an Agilent 7700x (Agilent Technologies, Santa Clara, CA, USA) inductively coupled plasma mass spectrometer (ICP-MS). Three reference standards (BCR-2, BHVO-1, and AGV-1) were measured during the course of the analytical procedure. The precision and accuracy values for most trace elements were better than 5% based on analyses of the standards.

### 3.2. Major and Minor Elements of Minerals

Major and minor element compositions of ruby and titanite were obtained via electron microprobe analysis (JEOL JXA 8100, JEOL Ltd., Tokyo, Japan) at the Institute of Geology and Geophysics, Chinese Academy of Sciences (IGGCAS), Beijing, China. Quantitative analyses of the titanite were performed using wavelength-dispersive spectrometers (WDS) with an acceleration voltage of 15 kV, a beam current of 20 nA, and a 5 µm beam size. The  $K\alpha$  characteristic X-rays of all elements were chosen for analysis. The following crystals were used: one PETJ crystal for K, Cl, Ca, and Ti; one LIFH crystal for Cr, Mn, Fe, and Ni; one TAP crystal for Na, Mg, Al, and Si; and one LDE1 crystal for F. The standards used were albite for Na; diopside for Si, Ca, and Mg; hematite for Fe; synthetic  $Cr_2O_3$  for Cr; synthetic  $TiO_2$  for Ti; orthoclase for K; fluorite for F; tugtupite for Cl; synthetic  $Al_2O_3$  for Al; synthetic MnO for Mn; and synthetic NiO for Ni. The peak counting time was 20 s for all elements except Fe, and the background counting time was 10 s at the high- and low-energy background positions. To lower the detection limit of Fe, the peak counting time of Fe was increased to 60 s. The detection limits ( $1\sigma$ ) were 145 µg/g for Na, 245 µg/g for F, 170 µg/g for Cr, 110 µg/g for K, 110 µg/g for Mg, 130 µg/g for Si, 140 µg/g for Mn, 95 µg/g for Cl, 100 µg/g for Al, 95 µg/g for Fe, 130 µg/g for Ca, 200 µg/g for Ni, and 190 µg/g for Ti. Titanite compositions were normalized on a three-cation basis and calculated on the basis of 5 (O, F) atoms. All Fe was calculated as  $Fe^{3+}$ .

For the major and minor element composition analyses of ruby, the beam current was increased to 50 nA. To lower the detection limits of Mg, Ti, V, Cr, Fe, and Ga, the peak counting times of these elements were increased to 60 s. The peak counting times for other elements remained at 20 s. The standards used were albite for Na, diopside for Si, Ca, and Mg, hematite for Fe, synthetic  $Cr_2O_3$  for Cr, synthetic  $TiO_2$  for Ti, orthoclase for K, synthetic  $Al_2O_3$  for Al, synthetic MnO for Mn, synthetic V metal for V, and synthetic GaAs for Ga. Under these conditions, the detection limits for ruby were 80 µg/g for Na, 50 µg/g for Cr, 27 µg/g for V, 100 µg/g for Ga, 55 µg/g for K, 42 µg/g for Mg, 70 µg/g for Si, 75 µg/g for Mn, 66 µg/g for Al, 48 µg/g for Fe, 65 µg/g for Ca, and 60 µg/g for Ti, based on  $1\sigma$  estimates of the measured background variance. All data were corrected online using a modified ZAF (atomic number, absorption, fluorescence) correction procedure. The precision and accuracy for major and minor elements were better than 2% based on analyses of the internal laboratory standards.

### 3.3. Trace Elements of Minerals

Ruby and titanite were carefully separated from ruby-bearing marble samples (13MK79 and 13MK80), handpicked under a binocular microscope, and mounted in epoxy resin. To identify the internal structures/zonation of the ruby and titanite, polished sections of ruby and titanite were carbon-coated for backscattered electron (BSE) images, undertaken on a JEOL JXA 8100 electron microprobe (15 kV) at IGGCAS. Both optical photomicrographs and BSE images were obtained to guide spot locations for analysis. Matrix titanite from thin sections and titanite inclusions in ruby from ruby resin were also selected for trace element analysis.

The trace element compositions of the ruby and titanite were analyzed using LA-ICP-MS at IGGCAS. All analytical spots in ruby and titanite mounts were selected to be free from visible inclusions and major fractures. Laser analyses were performed using an ArF

excimer laser ablation system (193 nm wavelength) coupled to an Agilent 7500a ICP-MS. For ruby, the analyses were conducted at an 8 Hz repetition rate with a 110  $\mu\text{m}$  beam diameter to enhance signals. For titanite, an 8 Hz repetition rate and 40  $\mu\text{m}$  spot size were used. The background and analysis counting times were 30 s and 60 s, respectively.  $^{27}\text{Al}$  was used as an internal standard for ruby and  $^{43}\text{Ca}$  was used for titanite. The NIST 610 glass standard was used as an external calibration and was measured twice at the beginning and end of each analytical batch (approximately eight analyses). The data calculations were done using GLITTER 4.0 Online Interactive Data Reduction for the LA-ICP-MS program developed by GEMOC, Macquarie University. The results acquired from the USGS rock standard (BCR-2G) showed that the analytic accuracy and reproducibility were generally better than 6% and 8%, respectively, for most trace elements.

### 3.4. Titanite U–Pb Dating

U–Th–Pb isotopes of separated titanite from ruby-bearing marble samples (13MK79 and 13MK80) were measured using SIMS (CAMECA IMS 1280-HR, CAMECA, Gennevilliers, France). During the analysis, mineral inclusions and major fractures were avoided according to the optical photomicrographs and BSE images. The analytical procedures were similar to those described by Ling et al. [22]. The  $\text{O}_2^-$  primary ion beam was accelerated at 13 kV, with an intensity of 10 nA and an analytical spot size of 20  $\mu\text{m} \times 30 \mu\text{m}$ . A mass resolution of approximately 7000 (defined at 50% peak height) was used. A single-electron multiplier was used in ion-counting mode to measure secondary ion beam intensities via a peak jumping sequence, including isotopes of  $\text{Pb}^+$ ,  $\text{Th}^+$ ,  $\text{U}^+$ ,  $\text{ThO}^+$ ,  $\text{UO}^+$ , and  $^{40}\text{Ca}^{48}\text{Ti}_2^{16}\text{O}_4^+$ , to produce one set of data. U–Pb ratios, absolute abundances, and matrix corrections were determined relative to the titanite standard YQ82 ( $^{206}\text{Pb}/^{238}\text{U}$  age =  $1837.6 \pm 1.0$  Ma, U = 60  $\mu\text{g}/\text{g}$ ,  $\text{Fe}_2\text{O}_3$  = 0.85 wt.%) [46,47], analyses of which were interspersed with those of the unknown grains. To monitor the external uncertainties of the SIMS titanite U–Pb dating results, a secondary reference material, Ontario titanite, was alternately analyzed as an unknown together with other titanite samples. Seven measurements on Ontario titanite (Table S1) yielded an average  $^{206}\text{Pb}/^{238}\text{U}$  age of  $1050 \pm 15$  Ma (2se (standard error);  $n = 7$ ), which was within the error of the recommended value of  $1053.5 \pm 3.1$  Ma [19]. The SIMS U–Th–Pb data were processed using the program IsoPlot/Ex v. 2.49 [48]. The Tera–Wasserburg plot was constructed with common uncorrected lead data to deduce the common lead composition [49]. The  $^{207}\text{Pb}$ -based common Pb correction method was used, and the common lead composition used herein is the Pb isotopic composition regressed from sample data. Uncertainties in individual analyses are reported at the  $1\sigma$  level. The calculated intercept ages are quoted at the 95% confidence level, including uncertainties in calibration against the mineral standards.

## 4. Results

### 4.1. Whole-Rock Compositions

Whole-rock data for the major and trace elements are presented in Supplementary Table S2. The ruby-bearing marbles had high CaO contents (54.60–55.90 wt.%) and LOI (loss on ignition) values (42.19–43.76 wt.%) and contained minor amounts of  $\text{SiO}_2$  (0.30–1.30 wt.%),  $\text{TiO}_2$  (0.01–0.05 wt.%),  $\text{Al}_2\text{O}_3$  (0.18–1.10 wt.%),  $\text{MgO}$  (0.34–0.47 wt.%),  $\text{FeO}$  (0.10–0.39 wt.%), and  $\text{Fe}_2\text{O}_3$  (0.11–0.53 wt.%). The marbles had relatively high contents of large ion lithophile elements (LILEs) such as Ba (20  $\mu\text{g}/\text{g}$ ), Sr (171–261  $\mu\text{g}/\text{g}$ ), and Pb (8.1–9.6  $\mu\text{g}/\text{g}$ ). By comparison, ruby-bearing marbles contained low contents of high field strength elements (HFSEs, e.g., 0.4–1.2  $\mu\text{g}/\text{g}$  for Nb), rare earth elements (REEs, e.g., 3.5–7  $\mu\text{g}/\text{g}$  for La), and transition metal elements (TMEs, e.g., 10–20  $\mu\text{g}/\text{g}$  for Cr).

### 4.2. Mineral Chemistry

The representative major and minor element compositions of ruby are presented in Supplementary Table S3. Ruby contains a relatively wide range of  $\text{Cr}_2\text{O}_3$  contents (0.05 to 1.1 wt.%) but low contents of FeO, MnO, and  $\text{K}_2\text{O}$  (below the detection limit of EPMA).

Trace element compositions of ruby are presented in Supplementary Table S4. All elements listed were above the detection limit. The studied ruby had Cr contents of 249–2742 µg/g, V contents of 36.4–364 µg/g, Ti contents of 55.0–450 µg/g, and Fe contents of 35.9–584 µg/g. In addition, the ruby contained relatively low amounts of Mg (30.0–129 µg/g), Si (1099–1771 µg/g), Ca (543–1099 µg/g), and Ga (32.4–91.0 µg/g).

The representative major and minor element compositions of titanite are shown in Supplementary Table S5, and representative trace elements of titanite are listed in Supplementary Table S6. The matrix titanite and titanite inclusions showed the same composition characteristics (Figure S2). Both types showed low contents of Al<sub>2</sub>O<sub>3</sub> (2.94–3.42 wt.%) and low contents of Fe<sub>2</sub>O<sub>3</sub> (<0.05 wt.%). The F contents of titanite ranged from 0.93 to 1.10 wt.%. The trace element contents of these two types of titanite were similar, such as 633–760 µg/g Nb contents for matrix titanite and 643–664 µg/g Nb contents for titanite inclusions. In addition, these two types of titanite had similar LREE/HREE and Eu\* values and exhibited identical REE patterns (Figure S2d). The HFSE contents of the studied titanite were relatively high (e.g., Nb: 633–760 µg/g; Zr: 980–2174 µg/g). Moreover, the titanite had high contents of Th (150–271 µg/g) and U (572–826 µg/g) and low Th/U ratios of 0.19 to 0.42, with an average of 0.33. The contents of REEs ranged from 33.4 µg/g to 48.8 µg/g. The studied titanite was relatively enriched in LREEs (e.g., 3.21 µg/g for La) and depleted in HREEs (e.g., 0.14 µg/g for Lu). REE patterns generally exhibited flat shapes in the chondrite-normalized diagram with slight negative Eu anomalies (Eu/Eu\* = 0.51 – 0.69).

Separated titanite grains from ruby-bearing marble exhibited compositional features identical to those of matrix titanite and titanite inclusions. The variation in major and minor elements, such as contents of Al<sub>2</sub>O<sub>3</sub> (2.61–3.86 wt.%), Fe<sub>2</sub>O<sub>3</sub> (0.04–0.09 wt.%) and F (0.92–1.16 wt.%), was the same as that in the matrix titanite and titanite inclusions. The variation in the separated titanite was within the range of each trace element of the matrix titanite and titanite inclusions. For example, the representative Nb contents of the separated titanite were 677–1293 µg/g, which were similar to those of the matrix titanite (633–760 µg/g) and titanite inclusions (643–664 µg/g). In addition, element ratios such as Nb/Ta ratios varied in the same range (e.g., 5.93–23.1 for separated titanite, 15.7–20.8 for matrix titanite, and 13.1–15.0 for titanite inclusions). Moreover, the total amount of REEs in the separated titanite (30.4–178 µg/g) also fell in the variation range of matrix titanite (44.3–48.8 µg/g) and titanite inclusions (33.4–38.8 µg/g). The separated titanite also showed similar LREE/HREE and Eu\* values and exhibited REE patterns (Figure S2d) identical to those of matrix titanite in ruby-bearing marble and titanite inclusions in ruby.

#### 4.3. Titanite U–Pb Geochronology

The U–Th–Pb isotope data for Mogok titanite are presented in Table 1, and Tera–Wasserburg inverse U–Pb concordia plots (Figure 3) were constructed using common Pb uncorrected data. The titanite had relatively high U contents of 379–1858 µg/g and Th contents of 163–1004 µg/g. The Th/U values of titanite were between 0.1 and 1.1. Fifteen analyses of 13MK79 titanite yielded lower intercept ages of  $25.15 \pm 0.24$  Ma (MSWD = 0.26), and the Y intercept of the common <sup>207</sup>Pb/<sup>206</sup>Pb composition was  $0.86 \pm 0.20$ . Nineteen analyses of 13MK80 titanite yielded lower intercept ages of  $25.06 \pm 0.22$  Ma (MSWD = 0.15), and the Y intercept of the common <sup>207</sup>Pb/<sup>206</sup>Pb composition was  $0.83 \pm 0.10$  (Figure 3). With these common lead compositions, common Pb correction was conducted via the <sup>207</sup>Pb-based method. The <sup>207</sup>Pb-corrected weighted <sup>206</sup>Pb/<sup>238</sup>U ages for the two analyzed samples were  $25.14 \pm 0.25$  Ma (N = 15, MSWD = 0.25) and  $25.05 \pm 0.23$  Ma (N = 19, MSWD = 0.14), respectively, which were consistent with the lower intercept ages.

**Table 1.** U–Th–Pb analytical results of titanite in ruby-bearing marbles from the Mogok Stone Tract.

Sample/ Spot #	[U] µg/g	[Th] µg/g	Th/U	<sup>238</sup> U <sup>206</sup> Pb	±s %	<sup>207</sup> Pb <sup>206</sup> Pb	±s %	<sup>207</sup> Pb-corr age (Ma)	±s (Ma)	f <sub>206</sub> %
13MK79-1	1159	897	0.8	228	1.9	0.134	0.8	25.04	0.53	{11.35}
13MK79-2	1433	279	0.2	248	1.9	0.085	1.0	24.72	0.48	{5.46}
13MK79-3	1141	170	0.1	239	2.0	0.096	1.1	25.22	0.50	{7.46}
13MK79-4	1192	279	0.2	241	1.9	0.089	1.0	25.25	0.50	{5.53}
13MK79-5	1136	290	0.3	243	1.9	0.093	1.2	24.86	0.48	{7.32}
13MK79-6	1155	252	0.2	240	1.9	0.089	1.0	25.38	0.49	{5.97}
13MK79-7	629	197	0.3	230	1.9	0.127	1.1	25.14	0.51	{11.45}
13MK79-8	1027	622	0.6	238	1.9	0.096	1.0	25.38	0.49	{7.80}
13MK79-9	1211	180	0.1	240	1.9	0.090	1.0	25.36	0.49	{6.03}
13MK79-10	1108	530	0.5	240	1.9	0.090	1.1	25.37	0.49	{5.89}
13MK79-11	900	569	0.6	239	1.9	0.108	1.1	24.82	0.49	{7.21}
13MK79-12	1224	575	0.5	245	1.9	0.093	1.0	24.75	0.48	{6.44}
13MK79-13	1229	419	0.3	243	1.9	0.082	1.0	25.30	0.48	{4.96}
13MK79-14	1208	397	0.3	242	1.9	0.086	1.2	25.27	0.49	{4.31}
13MK79-15	578	396	0.7	231	1.9	0.119	1.6	25.31	0.51	{10.69}
13MK80-1	1305	222	0.2	241	1.9	0.087	1.2	25.28	0.49	{5.63}
13MK80-2	1217	399	0.3	243	1.9	0.091	1.0	24.98	0.48	{5.65}
13MK80-3	1412	163	0.1	245	1.9	0.090	1.0	24.78	0.48	{6.75}
13MK80-4	1858	451	0.2	248	2.0	0.075	0.9	24.97	0.49	{3.95}
13MK80-5	1323	275	0.2	241	2.0	0.084	1.1	25.37	0.50	{5.31}
13MK80-6	1233	263	0.2	243	1.9	0.090	1.0	25.01	0.48	{6.82}
13MK80-7	1122	399	0.4	243	1.9	0.087	1.2	25.07	0.48	{4.65}
13MK80-8	1223	764	0.6	234	1.9	0.115	0.9	25.08	0.51	{8.29}
13MK80-9	879	249	0.3	237	1.9	0.107	1.3	25.05	0.50	{11.13}
13MK80-10	1456	233	0.2	243	1.9	0.084	0.9	25.23	0.49	{5.15}
13MK80-11	1337	273	0.2	245	1.9	0.087	1.1	24.86	0.48	{5.74}
13MK80-12	1191	1004	0.8	230	1.9	0.119	0.9	25.35	0.51	{9.75}
13MK80-13	1384	303	0.2	245	1.9	0.089	1.0	24.80	0.49	{5.56}
13MK80-14	1219	579	0.5	242	1.9	0.093	1.0	25.00	0.48	{6.46}
13MK80-15	1160	506	0.4	242	1.9	0.093	1.0	25.04	0.49	{7.73}
13MK80-16	1328	257	0.2	246	2.0	0.084	1.2	24.90	0.50	{6.18}
13MK80-17	1160	807	0.7	226	1.9	0.148	1.3	24.82	0.53	{13.80}
13MK80-18	1122	317	0.3	239	1.9	0.094	1.4	25.32	0.49	{6.62}
13MK80-19	379	412	1.1	220	1.9	0.155	1.9	25.20	0.55	{13.76}

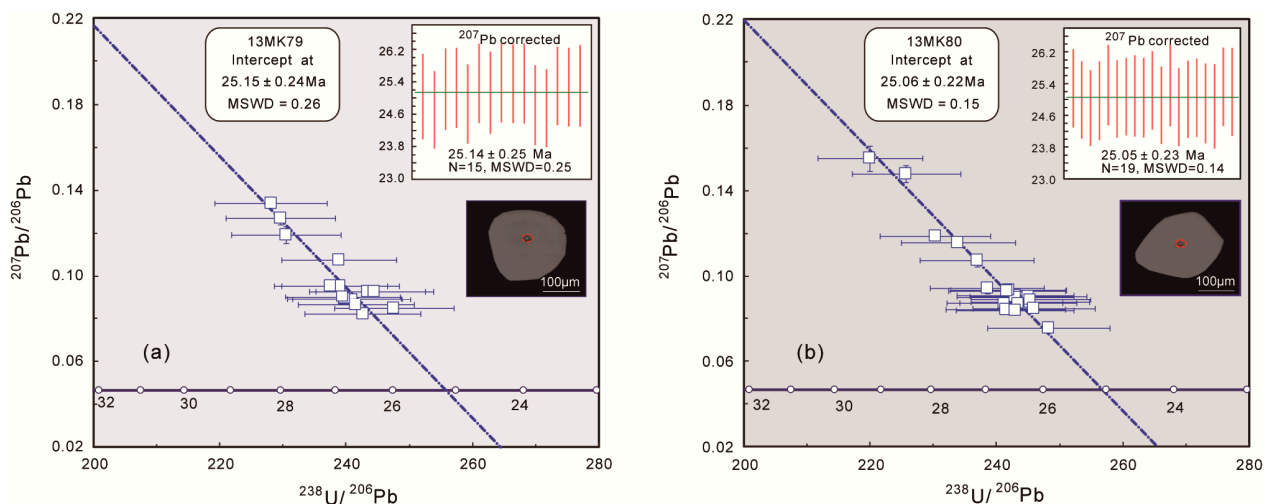


**Figure 3.** Tera–Wasserburg inverse U–Pb concordia diagrams for titanite from two ruby-bearing marbles from the Mogok Stone Tract. Data point error bars are at the  $2\sigma$  level. (a) Tera–Wasserburg inverse U–Pb concordia diagram for titanite from ruby-bearing marble (13MK79). (b) Tera–Wasserburg inverse U–Pb concordia diagram for titanite from ruby-bearing marble (13MK80).

## 5. Discussion

### 5.1. Chemical Characteristics of the Studied Ruby

Trace elements in ruby can provide important insights into their genesis characteristics and crystallization conditions [4]. Several detailed studies have investigated the trace element characteristics of Mogok ruby and attempted to determine the “fingerprint” features from particular lithological sources [2,4,12,43,50–52], especially the following elements that can be substituted for  $\text{Al}^{3+}$  in the crystal structure: Cr, Fe, V, Ti, Mg, and Ga. For example, Giuliani et al. [53] and Uher et al. [54] determined that the  $\text{FeO} + \text{TiO}_2 + \text{Ga}_2\text{O}_3$  versus  $\text{FeO}-\text{Cr}_2\text{O}_3-\text{MgO}-\text{V}_2\text{O}_3$  diagram (Figure 4a) may be used to classify the gem corundum into genetic fields related to host rock type associations, based on more than 2000 EPMA analyses of ruby and sapphire that were obtained under the same analytical conditions. Thus, nearly all Thurein Taung ruby from the Mogok Stone Tract was in the ruby-in-marble field [12]. In addition, a statistical classification via discriminant factor (Figure 4b) analysis using these element oxide concentrations can also be used to separate various gem corundum deposits [53]. Moreover, Harlow and Bender [4] emphasized the importance of Cr, V, and Fe in distinguishing ruby genesis, and they found that the composition of Mogok ruby plotted in a marble-hosted field showed some overlap in the metasomatic/metamorphic field in the Fe vs. Cr diagram (Figure 4c) and V vs. Cr diagram (Figure 4d). In addition, Zaw et al. [43] emphasized that the parameters  $(\text{V} + \text{Cr})/\text{Ga}$  and  $\text{Fe}/\text{Ti}$  can help to distinguish the ruby formation process based on the finding that ruby from metamorphic and metasomatic suites typically has higher Cr and lower Fe and Ga contents than that from magmatic suites [55,56]. Their results stressed that ruby samples from the Mogok Stone Tract have a metamorphic affiliation (Figure 4e). On the basis of the differences in V contents between ruby and sapphire, Zaw et al. [43] also classified corundum minerals into four types: low-V ( $<35 \mu\text{g/g}$ ), intermediate-V ( $35\text{--}90 \mu\text{g/g}$ ), high-V ( $>90 \mu\text{g/g}$ ) types, and extreme-V values ( $>1000 \mu\text{g/g}$ ). Sutherland et al. [50] also proposed that  $\text{Fe}/\text{Mg}$  vs.  $\text{Ga}/\text{Mg}$  plots (Figure 4f) can be used to identify metamorphic or magmatic corundum.

Here, we compared our results with published data on Mogok ruby. The element oxide plots show that the studied ruby samples were plotted into the ruby-in-marble field (Figure 4a,b). In addition, our results indicate that the studied Mogok ruby samples contained relatively high Cr contents of  $249\text{--}2742 \mu\text{g/g}$  and relatively low Fe contents of  $35.9\text{--}584 \mu\text{g/g}$ , which are very similar to previous reports on Mogok ruby (Figure 4c). The ruby samples had high V contents of  $36.4\text{--}364 \mu\text{g/g}$ , among which nearly 80% of the samples had V contents above  $90 \mu\text{g/g}$  (Table S4). Most ruby was plotted in the marble-hosted field in the V vs. Cr plot (Figure 4d). The  $(\text{V} + \text{Cr})/\text{Ga}$  and  $\text{Fe}/\text{Ti}$  ratios of ruby ranged from 7.19 to 63.79 and from 0.23 to 2.08, respectively. Moreover, the  $\text{Fe}/\text{Mg}$  and  $\text{Ga}/\text{Mg}$  ratios of ruby ranged from 1.07 to 7.11 and from 0.61 to 1.57, respectively. Based on the results of Zaw et al. [43] and Sutherland et al. [50], the investigated ruby samples exhibited a metamorphic origin (Figure 4e,f).

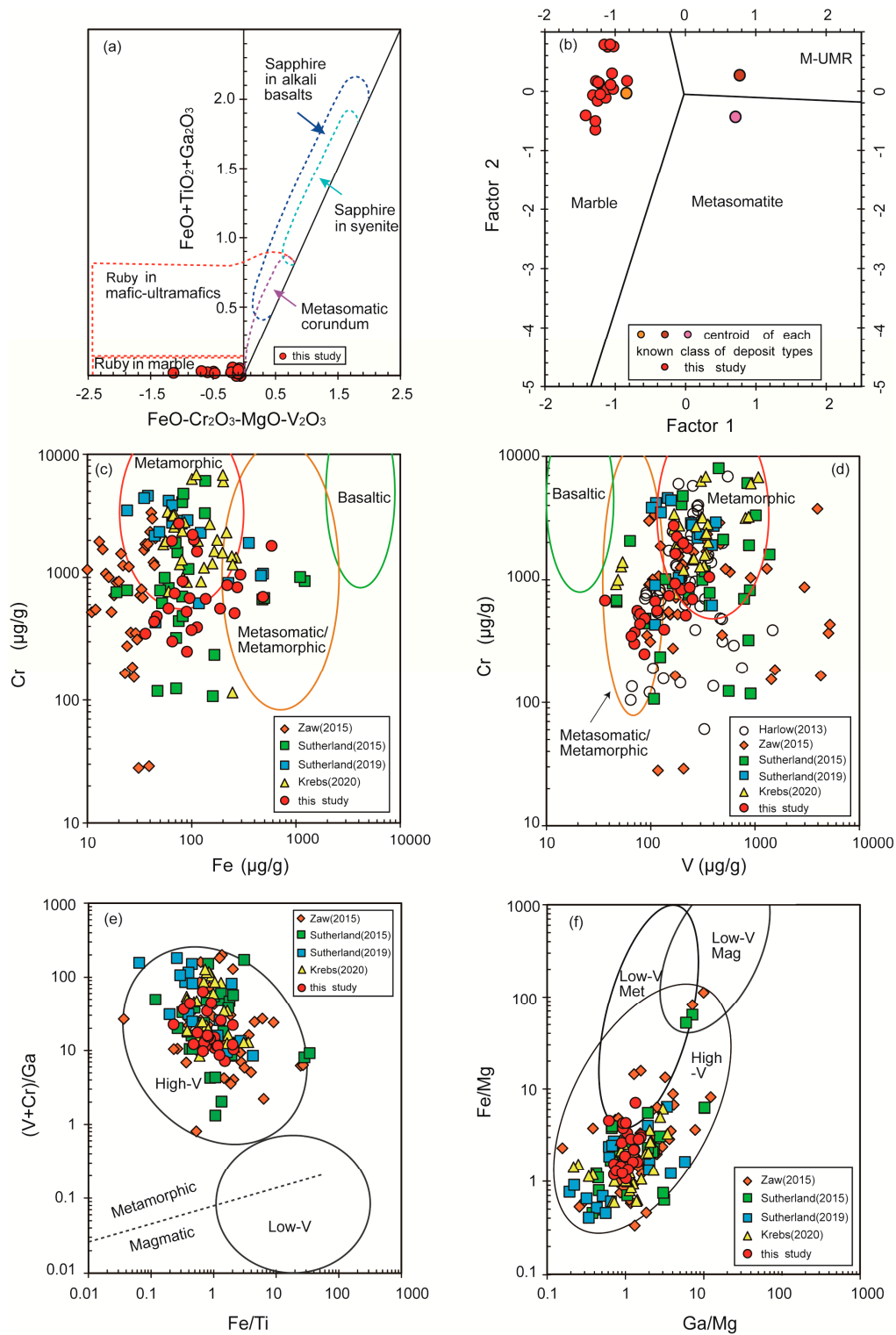


**Figure 4.** V, Cr, Fe, Ti, Ga, and Mg relationships for ruby from Mogok. (a) Discrimination metal oxide plots, with petrological fields after [53], for the studied samples. (b) Discriminant factor analysis using oxide concentrations in ruby, modified from [53], for the studied samples. M-UMR: metamorphosed mafic and ultramafic rocks. (c) Fe vs. Cr plot. This plot was modified after [4,57]. (d) V vs. Cr plot (modified after [4]). (e) Fe/Ti vs. (V+Cr)/Ga plot. High-V means high-V metamorphic suite in Mogok and low-V means low-V metamorphic suites in Mogok. This plot was modified after [43]. (f) Ga/Mg vs. Fe/Mg plot (modified after [43,50]), Met: metamorphic, Mag: magmatic.

### 5.2. Chemical Characteristics of the Studied Titanite

Based on the results of mineral chemistry (Tables S5 and S6, Figure S2), matrix titanite and titanite inclusions in ruby exhibited the same chemical compositional characteristics. The studied titanite samples contained high CaO contents of 28.54–29.46 wt.%, which is close to the ideal pure stoichiometric compound, 28.5 wt.%. Based on the Al content at the octahedral site ( $0.093 \leq X_{Al} \leq 0.138$ ), the studied samples belonged to the low-aluminum titanite described by Oberti et al. [58,59]. The Fe<sub>2</sub>O<sub>3</sub> contents of titanite were below 0.09 wt.%, which may be relevant to the low FeO concentrations of the whole rock. Titanite samples had slightly higher F contents (0.90 to 1.16 wt.%). These data revealed a negative linear correlation between Ti and (Al + Fe<sup>3+</sup>) and a positive correlation between F and (Al + Fe<sup>3+</sup>) (Figure S2a,b), indicating the following substitution:  $(Fe, Al)^{3+} + (OH, F)^- \Leftrightarrow Ti^{4+} + O^{2-}$  [60]. Major element contents of the studied titanite samples were the same as those of titanite inclusions in ruby from Mogok [12] and titanite in ruby-bearing marble in Tanzania [1]. Moreover, the Fe/Al ratios of titanite were close to zero and the data points were close to the field of metamorphic titanite on the plot of Fe versus Al, implying a metamorphic genesis (Figure S2c).

The titanite samples generally exhibited a flat REE pattern with slight negative Eu anomalies (Figure S2d), similar to that of the titanite grains in ruby-bearing marble from Mogok [8]. The amount of REEs was 30.4–178 µg/g, which was slightly lower than the values determined for titanite inclusions (~1800 µg/g) in ruby from the MMB [12] but obviously lower than those (generally >10,000 µg/g) of igneous and hydrothermal titanite [61,62]. Moreover, the Th/U ratios of titanite ranged from 0.19 to 0.72 with an average of 0.45, lying in the Th/U ratio range (<1) for metamorphic titanite and distinctively different from magmatic titanite [21,22,61–64].

### 5.3. Ruby Formation Age in the MMB

The petrographic study of ruby-bearing marbles showed that titanite generally occurs in the matrix or as inclusions in ruby (Figure 2e,g,h). Geochemical results indicate that these two types of titanite exhibit the same chemical features (Figure S2), suggesting both types of titanite may form at the same metamorphic stage. Therefore, titanite is in equilibrium with ruby, which indicates that they form a stable assemblage, and thus presumably formed simultaneously. In addition, separated titanite, used for U–Pb dating, exhibited the same mineral chemical characteristics as matrix titanite and titanite inclusions in ruby, indicating that the ages constrained by separated titanite are consistent with the ages obtained for titanite inclusions in ruby. Moreover, because the formation temperatures of the gem-quality ruby in marble are close to the closure temperatures of the U–Pb system in titanite [14,23], the obtained U–Pb ages of titanite are suggested to represent the best constraints on the timing of ruby formation in Mogok.

In most cases, significant amounts of common Pb in titanite may introduce some issues in titanite U–Pb dating, the accuracy and reliability of which are often dependent on correction for common Pb [16,65,66]. However, the sample in this study contained a relatively low amount of common Pb, and the  $f_{206}$  was between 4.31% and 13.80%. Therefore, the results of this titanite are reliable, and we calculated the age of titanite by regression of uncorrected data on a Tera–Wasserburg plot. The SIMS titanite U–Pb dates from the ruby-bearing marble showed a component of common Pb with no overdispersion, which indicates that no temporal differences between the analyzed titanites could be distinguished at this analytical resolution [67]. The Y intercepts of the common <sup>207</sup>Pb/<sup>206</sup>Pb composition of the two samples were  $0.86 \pm 0.20$  and  $0.83 \pm 0.10$ , respectively, consistent with the evolution of global Pb [68] and reflecting the high accuracy and precision of the dating analysis.

Our new dating results (~25 Ma) are very similar to the newly reported formation ages for ruby from other deposits in the Mogok Stone Tract, including the youngest concordia age ( $22.26 \pm 0.36$  Ma) constrained from the rim of the zircon inclusion in gem-quality ruby [7] and the U–Pb titanite ages (~21 Ma) from the ruby-bearing marbles at the Le Oo

mine in the Mogok valley [8]. In addition, the newly obtained formation ages of ruby are slightly older than the previous Ar–Ar phlogopite cooling ages (17–18 Ma) of ruby-bearing marbles [6] which represents a younger age than ruby formation. However, our new dating results differ from the previous ages constrained from mineral inclusions (titanite and zircon: 31–32 Ma) [10–12], which may be related to different ruby formation processes and reflect various formation ages of ruby in the Mogok Stone Tract.

The mineralization age of the studied ruby deposit near Kyatpyin is in agreement with the timing of post-collisional extension in the Himalaya related to the migration of the eastern Himalayan syntaxis [5–7]. In addition, recent studies have reported a wide distribution of ~21–25 Ma for syenite and charnockite intrusions in the Mogok area [8,39], which induced high-temperature metamorphism or metasomatism in the marbles. We thus suggest that the formation of the studied ruby deposit near Kyatpyin is most likely related to the Miocene–Oligocene high-grade metamorphic event during the India–Asia collision.

Based on the various dating results of ruby formation age, we infer that ruby in the Mogok Stone Tract may have formed at different periods of time from the Miocene to the Oligocene, probably via different formation processes. A titanite inclusion from Thurein Taung provided a U–Pb date of ~32 Ma [12], which may be connected to the adjacent leucogranites. The same results (31–32 Ma) were acquired for zircon inclusions in Mogok ruby [10,11]. Younger ruby formation ages (21–22 Ma) are also constrained by titanite in ruby-bearing marble [8] and zircon inclusions [7]. Searle et al. [8] found that ruby was spatially related to a series of charnockite-syenite sill-like intrusions around the Mogok valley and that the U–Pb titanite ages (~21 Ma) from ruby marbles and skarns at the Le Oo mine were similar to titanite ages from an adjacent syenite (22 Ma). They suggested that the intrusion of syenites was affected by regional granulite-facies metamorphism lasting from ~68–21 Ma, and thus ruby was formed during this regional metamorphic episode by granulite-facies metamorphism of skarns and thick marbles. Phyo et al. [7] reported the youngest ages of zircon inclusions at  $22.26 \pm 0.36$  Ma and interpreted this age as the marble-hosted ruby formation time, which may be related to a regional granulite-facies metamorphic event. In addition, a zircon U–Pb date of 16.1 Ma in an extremely rare painite ( $\text{CaZrAl}_9\text{O}_{15}(\text{BO}_3)$ ) overgrowth on ruby in a skarn contact between leucogranite and marble (Wet Loo mine [39]) is the youngest ruby formation age reported to date. This age is in conjunction with the Kagaing granite (~16.8 Ma) [12,40] and the youngest zircon age in Bawlongyi marble [7]. These youngest ages are interpreted to be related to post-regional metamorphic contact metamorphism [39,40,69] caused by the late intrusion of nearby Kabaing granite [7]. To date, ruby formation timing exhibits a wide range from the Miocene to early Oligocene related to the complex magmatic/metamorphic events in the Mogok area. Regional high-grade granulite-facies metamorphism plays an important role in ruby formation. Due to the numerous ruby mines in the Mogok Stone Tract, more geochronological data are urgently needed to better understand the formation process and genesis of ruby in this famous region.

Moreover, ruby (and other corundum gemstones) is widely distributed in the Himalayan orogen and can be produced by disparate mechanisms, e.g., metasomatism [4,70], metamorphism of Al-rich calcareous rocks [71], and possible metamorphism of an evaporite-bearing carbonate platform [23]. Further chronological work is strongly needed to examine the timing of the mineralization of different deposit types along the Himalayan orogen. In this aspect, texturally constrained titanite could be a precise geochronometer to date the mineralization of different types of ruby.

## 6. Conclusions

Titanite occurs as a matrix mineral or ruby inclusions in ruby-bearing marbles from a ruby deposit near Kyatpyin in the Mogok Stone Tract, central Myanmar. Titanite provides important information on the origin and formation age of ruby.

These two types of titanite exhibit identical chemical compositions. Major, minor, and trace element characteristics reveal the metamorphic genesis of titanite. Ruby trace

elements show that the studied ruby has a metamorphic origin. In situ SIMS U–Pb dating on titanite yields ages of  $25.15 \pm 0.24$  Ma (MSWD = 0.26) and  $25.06 \pm 0.22$  Ma (MSWD = 0.15), suggesting a ~25 Ma ruby mineralization in the Mogok Stone Tract.

The studied ruby is most likely related to the high-temperature metamorphic event in the marbles during the India–Asia collision. Based on the various ruby formation ages previously reported, ruby in the Mogok area may have formed at different periods of time from the Miocene to the Oligocene, probably via different formation processes.

**Supplementary Materials:** The following are available online at <https://www.mdpi.com/article/10.3390/min11050536/s1>, Figure S1: Backscattered electron images showing accessory minerals in the ruby-bearing marbles, Figure S2: Mineral chemical features of the studied titanite samples. Table S1: U–Th–Pb analytical results of titanite standards, Table S2: Whole-rock compositions of the ruby-bearing marbles from the Mogok Stone Tract, Table S3: Representative EPMA results of ruby in studied samples (wt.%), Table S4: Representative trace elements compositions of ruby in studied samples ( $\mu\text{g/g}$ ), Table S5: Representative EPMA results of titanite in studied samples (wt.%), Table S6: Representative trace elements compositions of titanite in studied samples ( $\mu\text{g/g}$ ).

**Author Contributions:** S.G. and D.Z. developed the idea of this paper. D.Z. performed the analyses, interpreted the results of the analyses, and wrote the manuscript. S.G. substantially revised the original manuscript. S.G., Y.C. and C.L. collected the samples. Q.L. and X.L. provided technical input and assisted with the analyses. K.S. provided geology background. All authors contributed to discussion of the results and the writing of the paper. All authors have read and agreed to the published version of the manuscript.

**Funding:** This study was supported by the National Key Research and Development Program of China (2016YFE0203000), the National Natural Science Foundation of China (No. 41922013), the National Key Research and Development Program of China (2018YFA0702700), Youth Innovation Promotion Association CAS (2017090), the State Key Laboratory of Lithospheric Evolution (SKL-Z202002), and the Experimental Technology Innovation Fund (No.11990890) of the Institute of Geology and Geophysics, Chinese Academy of Sciences.

**Data Availability Statement:** The data presented in this study are available within the article.

**Acknowledgments:** We thank Tian Zhou for the help in geochemical analysis. We gratefully acknowledge five anonymous reviewers for their detailed comments and suggestions that help significantly improve the manuscript.

**Conflicts of Interest:** The authors declare no conflict of interest.

## References

1. Balmer, W.A.; Hauzenberger, C.A.; Fritz, H.; Sutthirat, C. Marble-hosted ruby deposits of the Morogoro Region, Tanzania. *J. Afr. Earth Sci.* **2017**, *134*, 626–643. [[CrossRef](#)]
2. Giuliani, G.; Groat, L.; Fallick, A.; Pignatelli, I.; Pardieu, V. Ruby deposits: A review and geological classification. *Minerals* **2020**, *10*, 597. [[CrossRef](#)]
3. Sotheby's Magnificent Jewels and Noble Jewels, Auction 502. 2005. Available online: <http://www.sothebys.com> (accessed on 28 July 2020).
4. Harlow, G.E.; Bender, W. A study of ruby (corundum) compositions from the Mogok Belt, Myanmar: Searching for chemical fingerprints. *Am. Miner.* **2013**, *98*, 1120–1132. [[CrossRef](#)]
5. Themelis, T. *Gems and Mines of Mogok*; A&T Pub.: Los Angeles, CA, USA, 2008.
6. Garnier, V.; Maluski, H.; Giuliani, G.; Ohnenstetter, D.; Schwarz, D. Ar–Ar and U–Pb ages of marble-hosted ruby deposits from central and southeast Asia. *Can. J. Earth Sci.* **2006**, *43*, 509–532. [[CrossRef](#)]
7. Phyo, M.M.; Wang, H.A.O.; Guillong, M.; Berger, A.; Franz, L.; Balmer, W.A.; Krzemnicki, M.S. U–Pb dating of zircon and zirconolite inclusions in marble-hosted gem-quality ruby and spinel from Mogok, Myanmar. *Minerals* **2020**, *10*, 195. [[CrossRef](#)]
8. Searle, M.P.; Garber, J.M.; Hacker, B.R.; Htun, K.; Gardiner, N.J.; Waters, D.J.; Robb, L.J. Timing of syenite–charnockite magmatism and ruby and sapphire metamorphism in the Mogok valley region, Myanmar. *Tectonics* **2020**. [[CrossRef](#)]
9. Wu, Y.B.; Zheng, Y.F.; Zhao, Z.F.; Gong, B.; Liu, X.M.; Wu, F.Y. U–Pb, Hf and O isotope evidence for two episodes of fluid-assisted zircon growth in marble-hosted eclogites from the Dabie orogen. *Geochim. Cosmochim. Acta* **2006**, *70*, 3743–3761. [[CrossRef](#)]
10. Zaw, K.; Sutherland, F.L.; Graham, I.T.; McGee, B. Dating zircon inclusions in gem corundums from placer deposits, as a guide to their origin. In Proceedings of the 33rd International Geological Congress (IGC), Oslo, Norway, 5–14 August 2008.

11. Zaw, K.; Sutherland, F.L.; Graham, I.T.; Meffre, S.; Thu, K. Dating zircon inclusions in gem corundum deposits and genetic implications. In Proceedings of the 13th Quadrennial IAGOD Symposium, Adelaide, Australia, 5–10 April 2010.
12. Sutherland, F.L.; Zaw, K.; Mere, S.; Thompson, J.; Goemann, K.; Thu, K.; Nu, T.; Zin, M.; Harris, S. Diversity in ruby geochemistry and its inclusions: Intra- and inter-continental comparisons from Myanmar and Eastern Australia. *Minerals* **2019**, *9*, 28. [[CrossRef](#)]
13. Belley, P.M.; Dzikowski, T.J.; Fagan, A.; Cempírek, J.; Groat, L.A.; Mortensen, J.K.; Fayek, M.; Giuliani, G.; Fallick, A.E.; Gertzbein, P. Origin of scapolite-hosted sapphire (corundum) near Kimmirut, Baffin Island, Nunavut, Canada. *Can. Miner.* **2017**, *55*, 669–699. [[CrossRef](#)]
14. Kohn, M. Titanite petrochronology. *Rev. Miner. Geochem.* **2017**, *83*, 419–441. [[CrossRef](#)]
15. Aleinikoff, J.N.; Wintsch, R.P.; Fanning, C.M.; Dorais, M.J. U–Pb geochronology of zircon and polygenetic titanite from the Glastonbury Complex, Connecticut, USA: An integrated SEM, EMPA, TIMS, and SHRIMP study. *Chem. Geol.* **2002**, *188*, 125–147. [[CrossRef](#)]
16. Storey, C.D.; Jeffries, T.E.; Smith, M. Common lead-corrected laser ablation ICP–MS U–Pb systematics and geochronology of titanite. *Chem. Geol.* **2006**, *227*, 37–52. [[CrossRef](#)]
17. Willigers, B.; Baker, J.A.; Krogstad, E.J.; Peate, D.W. Precise and accurate in situ Pb–Pb dating of apatite, monazite, and sphene by laser ablation multiple-collector ICP–MS. *Geochim. Cosmochim. Acta* **2002**, *66*, 1051–1066. [[CrossRef](#)]
18. Frost, B.R.; Chamberlain, K.R.; Schumacher, J.C. Sphene (titanite): Phase relations and role as a geochronometer. *Chem. Geol.* **2000**, *172*, 131–148. [[CrossRef](#)]
19. Spencer, K.J.; Hacker, B.R.; Kylander Clark, A.R.C.; Andersen, T.B.; Cottle, J.M.; Stearns, M.A.; Poletti, J.E.; Seward, G.G.E. Campaign-style titanite U–Pb dating by laser-ablation ICP: Implications for crustal flow, phase transformations and titanite closure. *Chem. Geol.* **2013**, *341*, 84–101. [[CrossRef](#)]
20. Li, Y.; Zhou, H.W.; Li, Q.L.; Xiang, H.; Zhong, Z.Q.; Brouwer, F.M. Palaeozoic polymetamorphism in the North Qinling orogenic belt, Central China: Insights from petrology and in situ titanite and zircon U–Pb geochronology. *J. Asian Earth Sci.* **2014**, *92*, 77–91. [[CrossRef](#)]
21. Rasmussen, B.; Fletcher, I.R.; Muhling, J.R. Dating deposition and low-grade metamorphism by in situ U–Pb geochronology of titanite in the Paleoproterozoic Timeball Hill Formation, southern Africa. *Chem. Geol.* **2013**, *351*, 29–39. [[CrossRef](#)]
22. Ling, X.X.; Schmädicke, E.; Li, Q.L.; Gose, J.; Wu, R.H.; Wang, S.Q.; Liu, Y.; Tang, G.Q.; Li, X.H. Age determination of nephrite by in-situ SIMS U–Pb dating syngenetic titanite: A case study of the nephrite deposit from Luanchuan, Henan, China. *Lithos* **2015**, *220–223*, 289–299. [[CrossRef](#)]
23. Garnier, V.; Giuliani, G.; Ohnenstetter, D.; Fallick, A.E.; Dubessy, J.; Banks, D.; Hoàng, Q.V.; Lhomme, T.; Maluski, H.; Pêcher, A.; et al. Marble-hosted ruby deposits from central and southeast Asia: Towards a new genetic model. *Ore Geol. Rev.* **2008**, *34*, 169–191. [[CrossRef](#)]
24. Mitchell, A.H.G. Cretaceous–Cenozoic tectonic events in the western Myanmar (Burma)–Assam region. *J. Geol. Soc. Lond.* **1993**, *150*, 1089–1102. [[CrossRef](#)]
25. Mitchell, A.H.G.; Htay, M.T.; Htun, K.M.; Win, M.N.; Oo, T.; Hlaing, T. Rock relationships in the Mogok metamorphic belt, Tatkon to Mandalay, central Myanmar. *J. Asian Earth Sci.* **2007**, *29*, 891–910. [[CrossRef](#)]
26. Searle, M.P.; Noble, S.R.; Cottle, J.M.; Waters, D.J.; Mitchell, A.H.G.; Hlaing, T.; Horstwood, M.S.A. Tectonic evolution of the Mogok metamorphic belt, Burma (Myanmar) constrained by U–Th–Pb dating of metamorphic and magmatic rocks. *Tectonics* **2007**, *26*. [[CrossRef](#)]
27. Bertrand, G.; Rangin, C. Tectonics of the western margin of the Shan plateau (central Myanmar): Implication for the India–Indochina Oblique convergence since the Oligocene. *J. Asian Earth Sci.* **2003**, *21*, 1139–1157. [[CrossRef](#)]
28. Liu, C.Z.; Chung, S.J.; Wu, F.Y.; Zhang, C.; Xu, Y.; Wang, J.G.; Chen, Y.; Guo, S. Tethyan suturing in Southeast Asia: Zircon U–Pb and Hf–O isotopic constraints from Myanmar ophiolites. *Geology* **2016**, *44*, 311–314. [[CrossRef](#)]
29. Barley, M.E.; Pickard, A.L.; Zaw, K.; Rak, P.; Doyle, M.G. Jurassic to Miocene magmatism and metamorphism in the Mogok metamorphic belt and the India–Eurasia collision in Myanmar. *Tectonics* **2003**, *22*, 1–11. [[CrossRef](#)]
30. Guo, S.; Chen, Y.; Liu, C.Z.; Wang, J.G.; Su, B.; Gao, Y.J.; Wu, F.Y.; Sein, K.; Yang, Y.H.; Mao, Q. Scheelite and coexisting F-rich zoned garnet, vesuvianite, fluorite, and apatite in calc–silicate rocks from the Mogok metamorphic belt, Myanmar: Implications for metasomatism in marble and the role of halogens in W mobilization and mineralization. *J. Asian Earth Sci.* **2016**, *117*, 82–106. [[CrossRef](#)]
31. Mitchell, A.; Chung, S.L.; Oo, T.; Lin, T.H.; Hung, C.H. Zircon U–Pb ages in Myanmar: Magmatic–metamorphic events and the closure of a neo–Tethys ocean? *J. Asian Earth Sci.* **2012**, *56*, 1–23. [[CrossRef](#)]
32. Searle, M.P.; Waters, D.J.; Morley, C.K.; Gardiner, N.J.; Htun, U.K.; Nu, T.T.; Robb, L.J. Chapter 12 Tectonic evolution of the Mogok metamorphic and Jade mines belts and ophiolitic terranes of Burma (Myanmar). In *Myanmar: Geology, Resources and Tectonics*; Barber, A.J., Zaw, K., Crow, M.J., Eds.; Geological Society: London, UK, 2017; Volume 48, pp. 261–293.
33. Chen, S.; Chen, Y.; Li, Y.B.; Su, B.; Zhang, Q.H.; Aung, M.M.; Sein, K. Cenozoic ultrahigh-temperature metamorphism in metapelitic granulites from the Mogok metamorphic belt, Myanmar. *Sci. China Earth Sci.* **2021**. [[CrossRef](#)]
34. Lamont, T.N.; Searle, M.P.; Hacker, B.R.; Htun, K.; Htun, K.M.; Morley, C.K.; Waters, D.J.; White, R.W. Late Eocene–Oligocene granulite facies garnet–sillimanite migmatites from the Mogok metamorphic belt, Myanmar, and implications for timing of slip along the Sagaing Fault. *Lithos* **2021**, *386–387*, 106027. [[CrossRef](#)]

35. Guo, S.; Chu, X.; Hermann, J.; Chen, Y.; Li, Q.L.; Wu, F.Y.; Liu, C.Z.; Sein, K. Multiple episodes of fluid infiltration along a single metasomatic channel in metacarbonates (Mogok metamorphic belt, Myanmar) and implications for CO<sub>2</sub> release in orogenic belts. *J. Geophys. Res. Solid Earth* **2021**, *126*, e2020JB020988. [[CrossRef](#)]
36. Win, M.M.; Enami, M.; Kato, T. Metamorphic conditions and CHIME monazite ages of Late Eocene to Late Oligocene high-temperature Mogok metamorphic rocks in central Myanmar. *J. Asian Earth Sci.* **2016**, *117*, 304–316. [[CrossRef](#)]
37. Thu, Y.K.; Enami, M.; Kato, T.; Tsuboi, M. Granulite facies paragneisses from the middle segment of the Mogok metamorphic belt, central Myanmar. *J. Miner. Petrol. Sci.* **2017**, *112*, 1–19.
38. Thu, Y.K.; Win, M.M.; Enami, M.; Tsuboi, M. Ti-rich biotite in spinel and quartz-bearing paragneiss and related rocks from the Mogok metamorphic belt, central Myanmar. *J. Miner. Petrol. Sci.* **2016**, *111*, 270–282.
39. Thu, K. The Igneous Rocks of the Mogok Stone Tract: Their Distribution, Petrography, Petrochemistry Sequence, Geochronology and Economic Geology. Ph.D. Thesis, University of Yangon, Yangon, Myanmar, 2007.
40. Gardiner, N.J.; Robb, L.J.; Morely, C.K.; Searle, M.P.; Cawood, P.A.; Whitehouse, M.J.; Kirkland, C.L.; Roberts, N.M.W.; Myint, T.A. The tectonic and metallogenic framework of Myanmar: A Tethyan mineral system. *Ore Geol. Rev.* **2016**, *79*, 26–45. [[CrossRef](#)]
41. Zaw, K. Geological evolution of selected granitic pegmatites in Myanmar (Burma): Constraints from regional setting, lithology, and fluid-inclusion studies. *Int. Geol. Rev.* **1998**, *40*, 647–662. [[CrossRef](#)]
42. Thein, M. Modes of occurrence and origin of precious gemstone deposits of the Mogok Stone Tract. *J. Myanmar Geosci. Soc.* **2008**, *1*, 75–84.
43. Zaw, K.; Sutherland, F.L.; Yui, T.F.; Mere, S.; Thu, K. Vanadium-rich ruby and sapphire within Mogok Gemfield, Myanmar: Implications for gem color and genesis. *Miner. Depos.* **2015**, *50*, 25–39. [[CrossRef](#)]
44. Whitney, D.L.; Evans, B.W. Abbreviations for names of rock-forming minerals. *Am. Miner.* **2010**, *95*, 185–187. [[CrossRef](#)]
45. Andrade, S.; Hypolito, R.; Ulbrich, H.H.; Silva, M.L. Iron (II) oxide determination in rocks and minerals. *Chem. Geol.* **2002**, *182*, 85–89. [[CrossRef](#)]
46. Li, Q.L.; Zhao, L.; Zhang, Y.B.; Yang, J.H.; Kin, J.N.; Han, R.H. Zircon-titanite-rutile U–Pb system from metamorphic rocks of Jungshan “Group” in Korea: Implications of tectono-thermal events from Paleoproterozoic to Mesozoic. *Acta Petrol. Sin.* **2016**, *32*, 3019–3032.
47. Ma, Q.; Evans, N.J.; Ling, X.X.; Yang, J.H.; Wu, F.Y.; Zhao, Z.D.; Yang, Y.H. Natural titanite reference materials for in situ U–Pb and Sm–Nd isotopic measurements by LA–(MC)–ICP–MS. *Geostand. Geoanal. Res.* **2019**, *43*, 355–384. [[CrossRef](#)]
48. Ludwig, K.R. *User’s Manual for Isoplot/Ex Rev. 2.49*; Berkeley Geochronology Centre Special Publication: Berkeley, CA, USA, 2001; p. 56.
49. Tera, F.; Wasserburg, G.J. U–Th–Pb systematics in three Apollo 14 basalts and the problem of initial Pb in lunar rocks. *Earth Planet Sci. Lett.* **1972**, *14*, 281–304. [[CrossRef](#)]
50. Sutherland, L.; Zaw, K.; Meffre, S.; Yui, T.–F.; Thu, K. Advances in trace element “fingerprinting” of gem corundum, ruby and sapphire, Mogok Area, Myanmar. *Minerals* **2015**, *5*, 61–79. [[CrossRef](#)]
51. Krebs, M.Y.; Hardman, M.F.; Pearson, D.G.; Luo, Y.; Fagan, A.J.; Sarkar, C. An evaluation of the potential for determination of the geographic origin of ruby and sapphire using an expanded trace element suite plus Sr–Pb isotope compositions. *Minerals* **2020**, *10*, 447. [[CrossRef](#)]
52. Palke, A.C. Coexisting rubies and blue sapphires from major world deposits: A brief review of their mineralogical properties. *Minerals* **2020**, *10*, 472. [[CrossRef](#)]
53. Giuliani, G.; Caumon, G.; Rakotosamizanany, S.; Ohnenstetter, D.; Rakotondrazafy, A.F.M. Classification chimique des corindons par analyse factorielle discriminante: Application à la typologie des gisements de rubis et saphirs. *Rev. Gemmol.* **2014**, *188*, 14–22.
54. Uher, P.; Giuliani, G.; Szakall, S.; Fallick, A.E.; Strunga, V.; Vaculovic, T.; Ozdin, D.; Greganova, M. Sapphires related to alkali basalts from the Cerová Highlands, Western Carpathians (southern Slovakia): Composition and origin. *Geol. Carp.* **2012**, *63*, 71–82. [[CrossRef](#)]
55. Pryce, M.H.L.; Runciman, W.A. The absorption spectrum of corundum. *Discuss Faraday Soc.* **1958**, *26*, 34–42. [[CrossRef](#)]
56. Sutherland, F.L.; Abduriyim, A. geographic typing of gem corundum: A test case from Australia. *J. Gemmol.* **2009**, *31*, 203–210. [[CrossRef](#)]
57. Calligaro, T.; Poirot, J.P.; Querré, G. Trace element fingerprinting of jewelry rubies by external beam PIXE. *Nucl. Instrum. Methods Phys. Res. B* **1999**, *150*, 628–634. [[CrossRef](#)]
58. Oberti, R.; Smith, D.C.; Rossi, G.; Caucia, F. The crystal chemistry of high-aluminium titanites. *Eur. J. Miner.* **1991**, *3*, 777–792. [[CrossRef](#)]
59. Oberti, R.; Rossi, G.; Smith, D.C. X-ray crystal structure refinement studies of the TiO || Al (OH, F) exchange in high aluminium spheens. *Terra Cogn.* **1985**, *5*, 428.
60. Higgins, J.B.; Ribbe, P.H. The crystal chemistry and space groups of natural and synthetic titanites. *Am. Miner.* **1976**, *61*, 878–888.
61. Gao, X.Y.; Zheng, Y.F.; Chen, Y.X.; Guo, J. Geochemical and U–Pb age constraints on the occurrence of polygenetic titanites in UHP metagranite in the Dabie orogen. *Lithos* **2012**, *136–139*, 93–108. [[CrossRef](#)]
62. Jiang, P.; Yang, K.F.; Fan, H.R.; Liu, X.; Cai, Y.C.; Yang, Y.H. Titanite-scale insights into multi-stage magma mixing in Early Cretaceous of NW Jiaodong terrane, North China Craton. *Lithos* **2016**, *258–259*, 197–214. [[CrossRef](#)]

63. Li, J.W.; Deng, X.D.; Zhou, M.F.; Liu, Y.S.; Zhao, X.F.; Guo, J.L. Laser ablation ICP–MS titanite U–Th–Pb dating of hydrothermal ore deposits: A case study of the Tonglushan Cu–Fe–Au skarn deposit, SE Hubei Province, China. *Chem. Geol.* **2010**, *270*, 56–67. [[CrossRef](#)]
64. Xiao, Y.Y.; Niu, Y.L.; Zhang, H.F.; Wang, K.L.; Lizuka, Y.; Lin, J.Y.; Tan, Y.L.; Xu, Y.J. Effects of decarbonation on elemental behaviors during subduction–zone metamorphism: Evidence from a titanite–rich contact between eclogite–facies marble and omphacite. *J. Asian Earth Sci.* **2017**, *135*, 338–346. [[CrossRef](#)]
65. Horstwood, M.S.A.; Foster, G.L.; Parrish, R.R.; Noble, S.R.; Nowell, G.M. Common–Pb corrected in situ U–Pb accessory mineral geochronology by LA–MC–ICP–MS. *J. Anal. At. Spectrom.* **2003**, *18*, 837–846. [[CrossRef](#)]
66. Simonetti, A.; Heaman, L.M.; Chacko, T.; Banerjee, N.R. In situ petrographic thin section U–Pb dating of zircon, monazite, and titanite using laser ablation–MC–ICPMS. *Int. J. Mass Spectrom.* **2006**, *253*, 87–97. [[CrossRef](#)]
67. Cao, M.J.; Qin, K.Z.; Evans, N.J.; Li, G.M.; Ling, X.X.; McInnes, B.I.A.; Zhao, J.X. Titanite in situ SIMS U–Pb geochronology, elemental and Nd isotopic signatures record mineralization and fluid characteristics at the Pusangguo skarn deposit, Tibet. *MD. Miner. Depos.* **2020**. [[CrossRef](#)]
68. Stacey, J.S.; Kramers, J.D. Approximation of terrestrial lead isotope evolution by a two–stage model. *Earth Planet Sci. Lett.* **1975**, *26*, 207–221. [[CrossRef](#)]
69. Bertrand, G.; Rangin, C.; Maluski, H.; Bellon, H. Diachronous cooling along the Mogok metamorphic belt (Shan scarp, Myanmar): The trace of the northward migration of the Indian syntaxis. *J. Asian Earth Sci.* **2001**, *19*, 649–659. [[CrossRef](#)]
70. Iyer, L.A.N. *The Geology and Gem–Stones of the Mogok Stone Tract, Burma. Memoirs of the Geological Survey of India*; Calcutta: Delhi, India, 1953; Volume 82.
71. Mitchell, A. Chapter 7 Mogok Metamorphic Belt. In *Geological Belts, Plate Boundaries, and Mineral Deposits in Myanmar*; Elsevier: Amsterdam, The Netherland, 2018; pp. 235–236.